Powder Technology 390 (2021) 62–72

Contents lists available at ScienceDirect

Powder Technology

journal homepage: www.elsevier.com/locate/powtec

Numerical investigation of powder aerosolization in a rotating drum apparatus

Hongyu Chen [c], Milind A. Jog [c], Douglas E. Evans [a], Leonid A. Turkevich [b,*]

[a] Health Effects Laboratory Division (HELD), National Institute for Occupational Safety & Health (NIOSH), The Centers for Disease Control & Prevention (CDC), Alice Hamilton Laboratory, 1090 Tusculum Avenue, Cincinnati, OH 45226, United States of America
[b] Division of Field Studies and Engineering (DFSE), National Institute for Occupational Safety & Health (NIOSH), The Centers for Disease Control & Prevention (CDC), Alice Hamilton Laboratory, 1090 Tusculum Avenue, Cincinnati, OH 45226, United States of America
[c] Thermal Fluids & Thermal Processing Laboratory, Mechanical & Materials Engineering, University of Cincinnati, Cincinnati, OH 45221-0072, United States of America

ARTICLE INFO

Article history:
Received 20 January 2021
Received in revised form 29 April 2021
Accepted 30 April 2021
Available online 29 May 2021

ABSTRACT

Essential to estimating the potential exposure from dusts of toxic, hazardous or irritant powders is the evaluation of the dustiness of the powders being handled. Dustiness is the tendency of a powder to aerosolize with a given input of energy. Evaluating dustiness of a manufactured powder can alert to a potential exposure to workers. It can also aid in the selection of manufacturing processes/operations which generate less dust for a particular substance and can provide vital information to guide selecting/creating powders which generate less dust. A widely used (but marginally understood) instrument to evaluate powder dustiness is the Rotating Drum. Using computational fluid dynamics, we have numerically investigated the flow inside the Rotating Drum dustiness tester during its operation. A complete description of the flow aerodynamics associated with operation of this instrument will assist in the interpretation of dustiness measurements conducted with this instrument.

1. Introduction

1.1. Dustiness

A variety of processes may generate airborne dust in the workplace [1]. These may include accidental spills [2], falling powders, via pouring or transferring processes [3], and other agitation of the powder, as in powder conveyance [4]. Grinding or milling of bulk materials also generates and suspends small particles as airborne dust [5]. Aerosolization of previously spilled or deposited powder (perhaps through cleanup) is also a potential dust source. The undesirable outcome is that a portion of the bulk powder becomes airborne.

1.1.1. Dustiness testing

Dustiness is 'the propensity of a material to generate airborne dust during its handling' [6,7]. While not a material property, powder dustiness is still quantifiable under a controlled testing protocol: application of a controlled mechanical or aerodynamic stimulus to disperse pre-existing particles from the test powder into the air [6,7].

Powders typically consist of primary particles, which are aggregated and then further agglomerated by adhesive binding forces. It is fairly easy to break up the loose agglomerates, while breaking up the aggregates into the primary particles often requires considerable mechanical action (e.g., via operations like ball milling); the fracture or further diminution of primary particle size can be achieved only with extreme difficulty.

In dustiness testing, the energy supplied is insufficient to divide the primary particles (which can only be achieved by grinding, cutting, or crushing), or even to break up the strongly bound aggregates of primary particles. However, the energy supplied is sufficient to separate agglomerates from the bulk powder.

Heitbrink et al. [8] correlated dustiness measurements and worker exposure in bag packing operations; dustiness was useful in predicting order of magnitude worker exposures. A simulated workplace study [9] of scooping/weighing/adding and cleaning/sweeping of powders found that dustiness was a major contributor to worker exposure. Dustiness testing has been used in the selection of appropriate dust controls [10]. Dustiness may also be relevant for assessing the potential risk of dust explosions [11–13a]. However, no clear relationship has yet been established linking inhalation exposure to dustiness [8,9,14–20].

1.1.2. Testing methods: falling powder, rotating drum, Venturi method

Various methods have been utilized to measure dustiness; for reviews, see [21–24]. Different organizations have adopted different standards [25–31].

In order to simulate various industrial procedures, dustiness testing has historically utilized configurations that have imparted fairly gentle

* Corresponding author.
E-mail address: LLT0@cdc.gov (L.A. Turkevich).

https://doi.org/10.1016/j.powtec.2021.04.102
0032-5910/

mechanical agitation to the powder. The aerodynamics of these configurations tend to involve large scale eddies.

In the continuous drop test [26,30], a bolus of particles is released from a height. The particles are aerosolized either by the countercurrents generated during the fall, or by the countercurrents generated by the impact of the bolus at the bottom of the fall [3,14,32–37]; the design utilized in EN 15051–3 [30] explicitly shields against this 'splash' contributing to the measured dustiness. This method has been used extensively by the Barcelona group [38–40].

In the rotating drum test [22,29], a powder is rotated within a drum with internal baffles, so that the substrate angle periodically increases; when the powder exceeds its angle of repose, a local avalanche ensues, which aerosolizes the particles [41–45]. A variant is the widely used Heubach method [27]. Historically, the Rotating Drum apparatus [29] has been used [45] for lower *Re* workplace (and mining) dustiness evaluation. Tsai et al. [46] have used the Rotating Drum to investigate the dustiness of nano-TiO_2 and fine ZnO, and, with extended sampling and increased rotation rates, they studied the particle size distributions of the aerosolized powders.

In both methods, aerosolization is gravity driven, possibly enhanced by agglomerate impact. The maximum particle velocities achievable by gravity are $v \sim (2gh)^{1/2}$–3 m/s, where h is the diameter of the drum.

These methods have been compared by various groups [6,47–51]. Aerosolization and dust generation under these conditions has also been modeled [52–54].

A qualitatively different method (Venturi Dustiness Test) was introduced [55] in order to test small quantities of pharmaceutical powders. Aerosolization of the powder occurs at high Reynolds number ($Re \sim 10^4$) within a tube, and the resulting aerosol is injected into, and then sampled from, an isolated chamber; particle velocities are v ~ 70 m/s. Venturi aerosolization proceeds under turbulent conditions, whereas in the gentle tests, the airflows are larger scale and are in the laminar regime [56].

NIOSH has used the Venturi instrument to measure the dustiness of 40 different powders [56], and also of pollens and molds [57]. Using computational fluid dynamics (CFD), Dubey et al. [58] describe the flow during injection and sampling phases of this instrument. Other CFD studies [59–61] have examined the aerosolization process within the tube. NIOSH is currently comparing [62] low *Re* (Rotating Drum) with high *Re* (Venturi) dustiness measurements.

1.2. Description of the rotating drum test apparatus

The rotating drum dustiness apparatus [29] consists of a cylindrical rotating drum (Fig. 1). During normal operation, the 300-mm diameter (electrically grounded) stainless steel drum rotates at $\omega = 4$ rpm. The drum has eight longitudinal vanes (length = 230 mm, height = 25 mm) to lift and let fall the powder under test. The drum is attached to a vacuum pump which induces an air flow rate of Q = 38 L/min (flow is left to right in the figure). The inlet air passes through a glass fiber filter to prevent dust contamination and to spread the incoming air flow across the diameter of the drum. The air exiting the apparatus passes through two size-selective foams and a filter to capture the powder particles that have been aerosolized. The inhalable, thoracic and respirable particle size fractions can thus be determined.

Test samples (nominal volume = 35 cm^3) are weighed and spread evenly along the bottom portion of the drum. At the end of the test, the outlet foams and filter are removed and weighed. The powder dustiness (for each size fraction) is the ratio of mass collected to the initial powder loading mass.

1.3. Other uses of the rotating drum configuration

The rotating drum configuration is widely used in industrial blending and mixing operations. As a result, there have been numerous studies to test the effectiveness of particle mixing in this geometry [63–68].

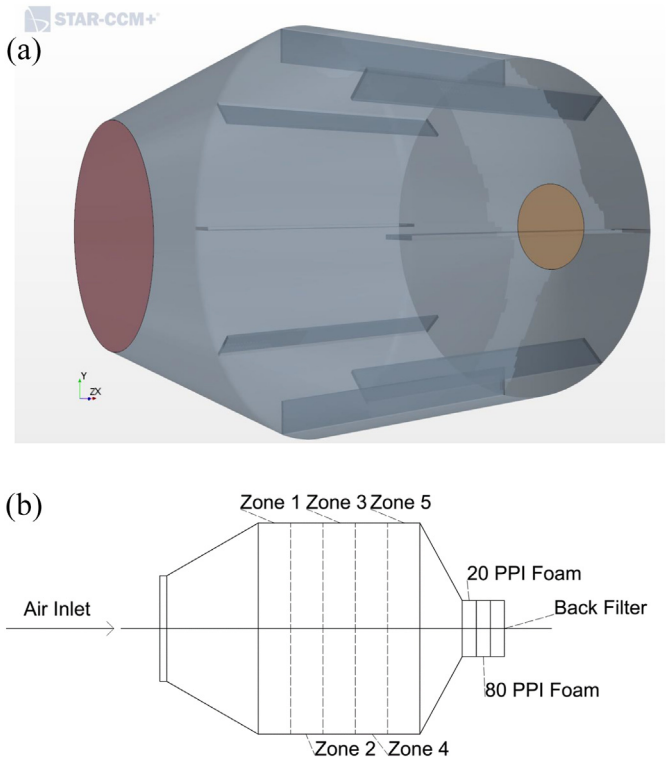

Fig. 1. a) Schematic, and b) model of the dustiness tester drum (European Standard EN15051–2).

Much work is devoted to particle segregation that occurs in this geometry [69–76].

Modeling of these processes has tended to emphasize the powder flow dynamics and hence simulates larger particles, primarily via DEM [77–83]. Modeling has been used to study segregation [84–90].

As an example, the Wollongong (Australia) group have conducted [91–93,95,99] Discrete Element Method (DEM) simulations of the Rotating Drum. These simulations model the behavior of large (d ~ mm) granules tumbling in the drum, in the absence of any air flow. The DEM simulations yield information on size and spatial segregation of particles within the rotating drum but are not appropriate for dust generation and transport (10 nm < d < 100 μm) in the presence of the test air flow.

By contrast, our work focuses on the aerosolization of small particles in the rotating drum geometry. As a result, we study smaller particles. We consider the dilute regime, so particle-particle interactions are neglected, in favor of the dominant air-particle interaction.

1.4. Summary of this work

The goal of this study was to conduct a numerical investigation of powder aerosolization and dust transport within the Rotating Drum Dustiness Apparatus. Computational fluid dynamics (CFD) simulation of air flow in the drum under normal operating conditions was carried out. A large number ($N \sim 10^2$) of particles were introduced at the bottom of the drum, and their motion was followed using a Lagrangian tracking technique. Based on the predicted particle paths, the number of particles leaving the drum (i.e. the particle capture efficiency) was determined. This particle capture efficiency was quantified in a second set of simulations ($N \sim 10^4$), where the particle trajectories are not retained, but where the final location of each particle (at the end of the simulated experiment) was monitored. Different particle sizes, from 1 nm to 30 μm diameters, were considered in the simulations in order to understand the effect of particle size on capture efficiency. Also, the

differences in particle motion based on their initial positions were studied. These computational results of flow aerodynamics and powder particle transport provide a better understanding of the operation of the drum dustiness tester and will help in interpreting measurements conducted using this apparatus.

Simulations have also been performed on a smaller, 'Danish' version of the European Standard, that is utilized in the experiments of Jensen et al. [51]. The results of these Danish drum simulations parallel those reported here (for the larger EN 15051–2 Standard) and are reported in the Supplemental Material. Simulations have also been carried out on the Heubach variant [27] of the Rotating Drum. In this protocol, a smaller drum is rotated at a faster rate and the volumetric air flows are larger, resulting in turbulent flow conditions within the drum. The axial jet wanders and is unstable, resulting in efficient turbulent mixing within the drum. While the instrument function still exhibits a cut-off for large particles ($d > 50$ μm), the Heubach version of the rotating drum is more efficient at measuring dust due to the smaller particles ($d < 8$ μm). The results of these simulations are sufficiently different from those of this study and therefore will be reported separately [96].

2. Numerical methods

2.1. Numerical simulation method (CFD)

We have used Star-CCM+ as the CFD simulation software in this study. Star-CCM+ can easily track massive particle trajectories. An implicit method was used to solve the unsteady governing equations.

2.1.1. Air flow only—No particles

At Q = 38 L/min, the nominal airflow Reynolds numbers are Re ~ 1140 at the inlet, 570 in the working section, 2140 at the exit of the drum. The rotation of the drum (with its internal fins) generates a slow swirl of this flow. Based on these Reynolds numbers ($\nu/c_{sound} < 10^{-3}$, where c_{sound} is the velocity of sound in air), the flow is described using incompressible continuity and laminar Navier-Stokes equations:

$$\frac{\partial(u_i)}{\partial x_i} = 0 \tag{1}$$

$$\frac{\partial(\rho u_i)}{\partial t} + \frac{\partial(\rho u_i u_j)}{\partial x_j} = -\frac{\partial p}{\partial x_i} + \frac{\partial}{\partial x_j}\left\{\mu\left(\frac{\partial u_i}{\partial x_j} + \frac{\partial u_j}{\partial x_i} - \frac{2}{3}\delta_{ij}\frac{\partial u_l}{\partial x_l}\right)\right\} \tag{2}$$

where u_i, denote averaged velocities.

The finite volume method (FVM) is used to discretize the governing equations. The discretization of equations and domain as well as the iterations of discretized equations are all conducted using commercial FVM solver STAR-CCM+. The convection terms are discretized using second-order Upwind Scheme. The transient terms are discretized by second-order Temporal Scheme. The time step is set at $\Delta t = 0.01$ s, and the simulation is run for $\Delta T = 60$ s (the total time of the dustiness experiment). The discretized governing equations are solved using the SIMPLE algorithm (Semi-Implicit Method for Pressure Linked Equations). Velocity and pressure under-relaxation factors are 0.8 and 0.2, respectively. Drum rotation is incorporated using rigid body motion of both the boundary and the grid. The solution of the equations was considered to be converged when the scaled residuals for the continuity and momentum equations decreased to 10^{-5} for each time step.

2.1.2. Addition of particles—Particle Tracking

Particles are injected at $t = 0$ (using the Star CCM+ Parcel Injector) with an initial velocity of $v = 1 \times 10^{-6}$ m/s. The parcel injectors are uniformly distributed at the bottom of the drum. Tracking of massive particles is incorporated via the Lagrangian-Euler Method with two-way coupling between air continuum and dispersed particulate phase; the two-way coupling eliminates the assumption that the particles follow the aerodynamic streamlines. Particle – particle interactions are neglected (volume fraction of the drum occupied by the powder is $\phi \sim 2 \times 10^{-3}$, so a fully dispersed aerosol would be dilute). Particle agglomeration and breakup are also neglected (aerodynamic shear forces are insufficient to drive agglomerate breakup; however, particle impact on the drum walls may induce breakup, and this has been neglected). Particle – drum wall interaction is modeled as pure elastic collision (i.e. unit coefficient of restitution), so no particles stick to the drum wall. This latter is definitely an approximation, as we have observed certain "less dusty" powders to adhere to the drum walls, whereas the "more dusty" powders exhibit less of an adherent dust layer on the drum surface at the end of the experiment.

In the Lagrangian-Euler Method, the motion of each dust particle in the Lagrangian frame is given by:

$$m_p \frac{dv_p}{dt} = F_d + F_p + m_p g \tag{3}$$

where m_p and v_p are the mass and velocity of the particle and g is the gravitational acceleration. The drag force, F_d, and pressure force, F_p, are given below. The drag force (in a direction opposite to the motion of the particle) is given by

$$F_d = \frac{1}{2} C_d \rho A_p v_r^2 \tag{4}$$

where $A_p = (\pi/2)\, D_p^2$ is the particle cross-sectional area, D_p is the particle diameter, ρ is the density of air, and the relative particle-air velocity $v_r = v - v_p$ where v is the local air velocity. The particle drag coefficient, C_d, is given by (Schiller-Naumann correlation [97]).

$$C_d = \frac{24}{Re_p}\left(1 + 0.15\, Re_p^{0.687}\right) \text{ for } Re_p < 1000$$

$$C_d = 0.44 \qquad \text{for } Re_p > 1000 \tag{5}$$

The particle Reynolds Number is defined by

$$Re_p = \frac{\rho |v_r| D_p}{\mu} \tag{6}$$

where μ is the viscosity of air. The pressure gradient force is given by

$$F_p = -V_p \nabla p_{static} \tag{7}$$

where $V_p = (\pi/6)\, D_p^3$ is the particle volume, and ∇p_{static} is the gradient of the static air pressure.

In two-way coupling, the rate of momentum transfer from the particles back to the continuum air phase is achieved by augmenting (2) with a sink term.

$$S_V = -\Sigma_n\, F_d^n\, \delta t_n / \Delta t \tag{8}$$

where the sum is over all particles n in the given cell during the computed time step, F_d^n is the drag force (4) exerted by the fluid on the n^{th} particle, and $\delta t/\Delta t$ is the fraction of time (typically~1) that the n^{th} particle spends in the given cell during this time step.

In order to simulate the experiments, the particles are initially distributed uniformly in a band at the bottom along the entire length of the drum, or confined to a shorter band within a specified zone; the azimuthal width of the band did not affect the results of the simulations.

2.2. Grid generation

Structured grids (surface lengths of 4, 3 and 2.2 mm) were generated within Star CCM+ for the cylindrical geometry; cells are cubes ('trimmed cells') in the bulk of the domain and flattened rectangular prisms at the boundary surface; half of the grid cells are situated in the five layers adjacent to the drum wall. The flows are not aggressive, so no refinement is necessary near the entrance and exit filters into/

Table 1
Computational grid details.

Cell base [mm]	Total boundary thickness [mm]	No. of boundary cells	Boundary growth factor	Cells	Faces	Vertices
4	0.73	5	1.1	482,696	1,418,207	485,414
3	1.0	5	1.0	1,104,824	3,257,696	1,104,993
2.2	1.33	4	1.1	2,631,612	7,789,350	2,629,990

out of the Rotating Drum volume. The grid rigidly rotates, anchored to the rotating drum wall. The basic grid parameters are listed in Table 1.

Shown in Fig. 2 is the finest (2.2 mm) grid: a) mid-section slice perpendicular to the axial direction, b) detail of this slice to elucidate the behavior of the grid near the outer radial boundary and the vanes (bulk grid at 45° angle with respect to the vane—the other trivial case is where the grid is aligned with the vane).

Grid independence [98] of the solutions is discussed in the Supplemental Material.

3. Experimental method

3.1. Equipment

The experiment was conducted in a standard dustiness rotating drum (European Standard EN15051–2, manufactured by JS Holdings, Stevenage, UK). Additional information on the dimensions and operation of the drum are contained in [29].

Air flows into the drum through a fiberglass filter, which, in addition to excluding background dust air contaminants, tends to spread out the entrance flow. The exit flow passes through two foams and a filter to size select the aerosolized dust: first a 20 ppi metalized foam (which excludes d > 10 μm), then an 80 ppi metalized foam (which excludes d > 4 μm), and finally a back filter.

The EN15051 standard specifies [29] that the powder is to be spread evenly along the length of the drum. For our experiments to determine the particle retention as a function of initial position of the powder particle, the base of the drum was divided into 5 zones, each of length 4.5 cm. Initial trial experiments determined that 35 mL of powder was excessive for coverage of a single zone; therefore, for these zonal experiments, 20 mL of powder were used. Fig. 3shows photographs of the powder in the interior of the drum, at the beginning and at the end of these zone loading experiments.

We also found a large humidity effect on the measured dustiness; thus multiple replicates had to be scheduled so as to sample all zones under the same humidity conditions. Additional trials (for better statistics) were conducted under different humidity conditions. In order to pool the data, we have looked at local efficiencies, compared to the average over all zones, measured on that day. This permits comparison between trials measured under different humidity conditions (41% < RH < 67%).

3.2. Materials

The standard EN 15051–3 requires 35 mL of powder for each run; our zonal experiments use 20 mL of powder for each zone (i.e. 100 mL of powder to sample the entire drum). The requirement of large quantities of material at uniform particle size is rather stringent. An additional requirement is that the dustiness of the material be reasonably large in order to be able to detect small changes in particle retention as a function of initial powder placement. For these experiments, we have used hollow fused borosilicate glass microspheres (ASTM C169) Sphericel® 110P8 (manufactured by Potters Industries LLC, Valley Forge, PA). Preliminary screening of materials indicated that this material has a (relatively large) dustiness of 8017 ± 1048 mg/kg. The nominal average size distribution is 9–13 μm (the manufacturer specifies 10% finer than 4–5 μm, 50% finer than 9–11 μm, 90% finer than 19–21 μm). The measured untapped powder density is $\rho_{powder} = 366 \pm 21$ kg/m^3. We also measured the moisture uptake $\Delta M/M = 0.16 \pm 0.04\%$ (as received vs. oven dried overnight at $T = 120$ °C) and $\Delta M/M = 0.16 \pm 0.04\%$ (conditioned at RH = 50% vs. oven dried overnight at T = 120 °C).

Fig. 4 is an SEM micrograph (ThermoFisher Scientific Phenom XL Desktop SEM with EDS attachment) of the Sphericel® powder. The powder is heterogeneous and consists primarily of two populations; the (number) majority at d ~ 3–5 μm, with a secondary population at d ~ 10–20 μm; there is also a tertiary population of irregular shards (l_{short} ~ 3 μm, l_{long} ~ 15 μm). Chemically, the small particles are consistent with a silicate, with elemental composition (given in atomic %) of Si (20 ± 1 at.%), O (71 ± 1 at.%), Na (8 ± 1 at.%), Ca (2 at.%); chemically, the large particles are augmented with significant carbon, with elemental composition of Si (11 ± 4 at.%), O (55 ± 4 at.%), C (30 ± 9 at.%), Na (4 ± 1 at.%), Ca (1 ± 1 at.%).

Based on the results of our simulations (Fig. 6 of Section 4.2.1), particles larger than 24 μm will not become aerosolized in the drum; hence, the experiments were compared with simulations of d ~ 5 μm microspheres (density $\rho = 1000$ kg/m^3 to reflect the hollow morphology).

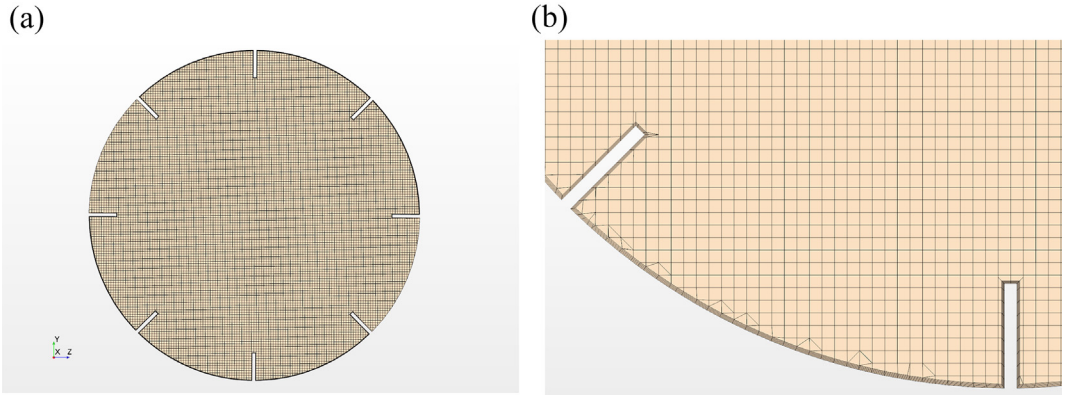

Fig. 2. Grid used: a) mid-section slice; b) detail near drum wall and vanes of mid-section slice.

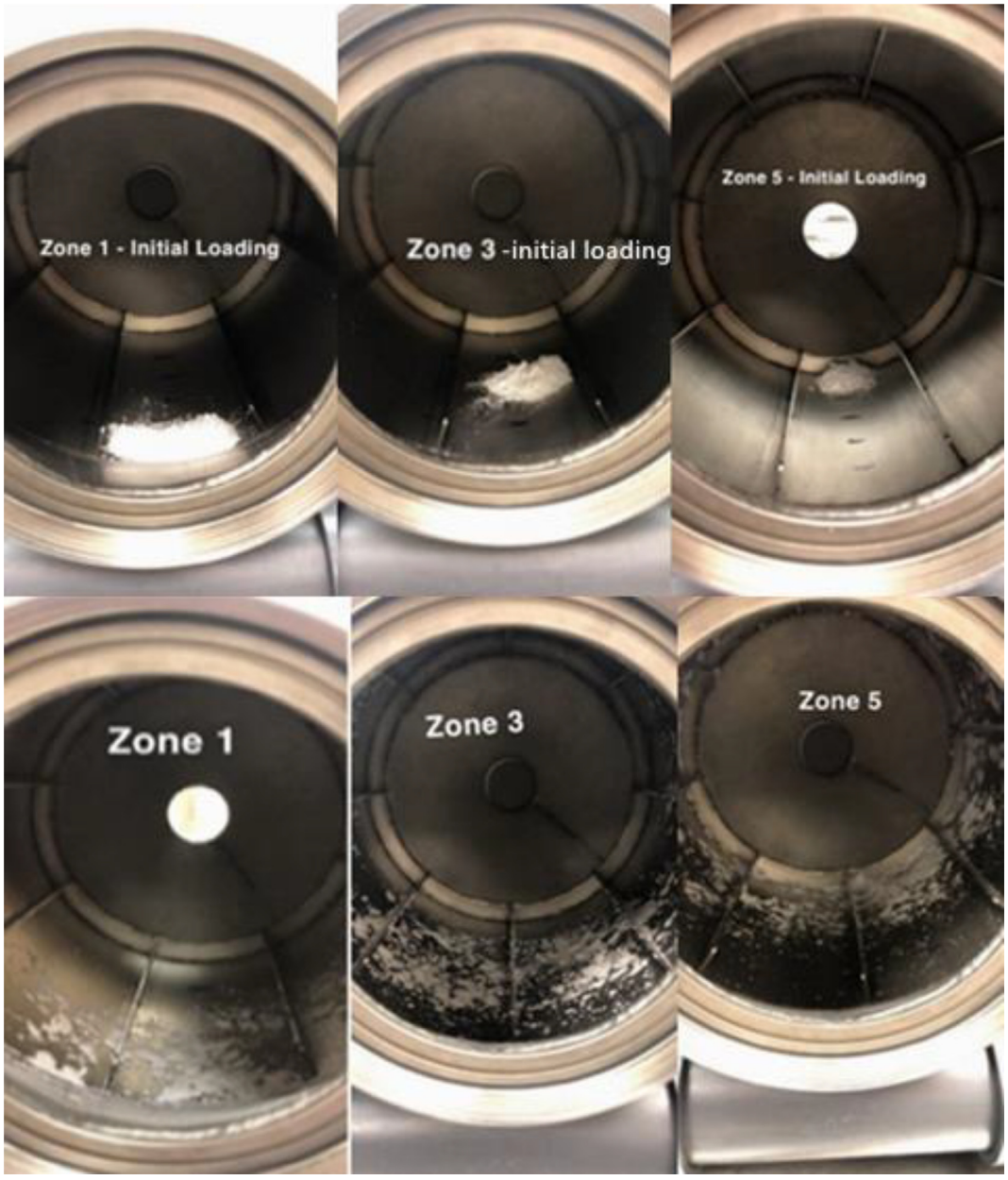

Fig. 3. Photographs of powder in the drum: top panel–at the start of the experiment $t = 0$ (left: zone 1; center: zone 3; right: zone 5); bottom panel—at the end of the experiment $t = 60$ s (left: powder having been loaded in zone 1; center: powder having been loaded in zone 3; right: powder having been loaded in zone 5).

4. Numerical results & discussion

4.1. Air flow without powder particles

Air flows into the Rotating Drum from the inlet in the direction of the rotational (horizontal) axis. The air flow expands in the inlet conical section, flows through the body of the drum, converges in the outlet conical section; the air exits the drum via outlet opening. The tangential air flow velocity vectors midway down the drum (at x = 0.222 m) are plotted in Fig. 5. The drum rotation is clockwise.

The flow exhibits an expected eight-fold symmetry. A helical flow pattern is generated in the central region while flow recirculates behind the vanes.

In the axial direction, the flow is characterized by a strong forward-directed axial flow along the center of the drum, with a weaker axial back-flow near the drum wall.

4.2. Simulations with air flows and particles

4.2.1. Particle capture efficiency

Simulations with monodisperse particles in the diameter range 100 nm < d < 30 μm were conducted (for each particle size, the simulation consisted of 10,000 particles). The overall capture efficiency (the fraction of particles that exits the drum during the 60 s test) at each diameter is plotted in Fig. 6 (results from the 4 mm grid):

For particle diameter d < 2 μm, ~ 30% of the particles escape the drum through the outlet surface, i.e. these particles are captured on the outlet filter and contribute to the measured dustiness. For particle diameter 2 μm < d < 10 μm, the capture efficiency slightly decreases and then drastically increases with the increase of particle diameter. The highest capture efficiency (> 90%) occurs when particle diameter d ~ 12.5 μm. For particle diameter d > 15 μm, the capture efficiency decreases quickly, and no particles escape for d > 24 μm. Thus, the

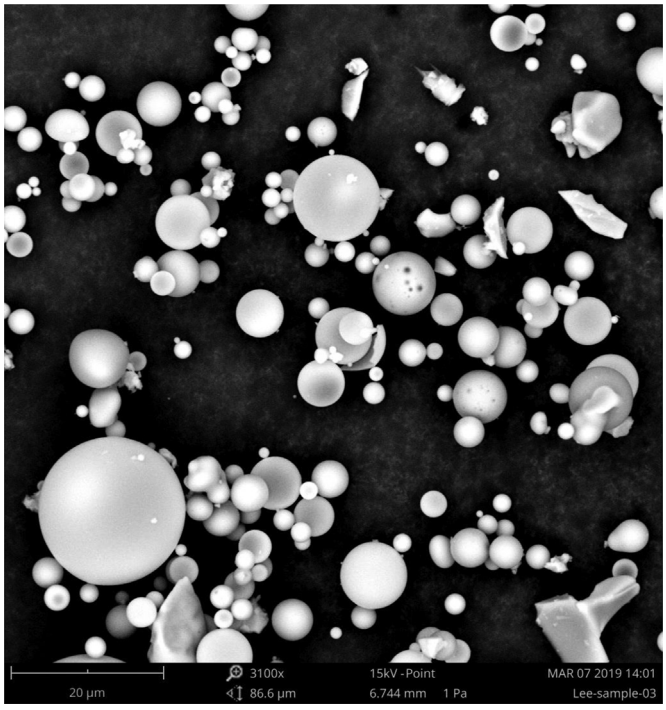

Fig. 4. SEM micrograph of Sphericel® powder.

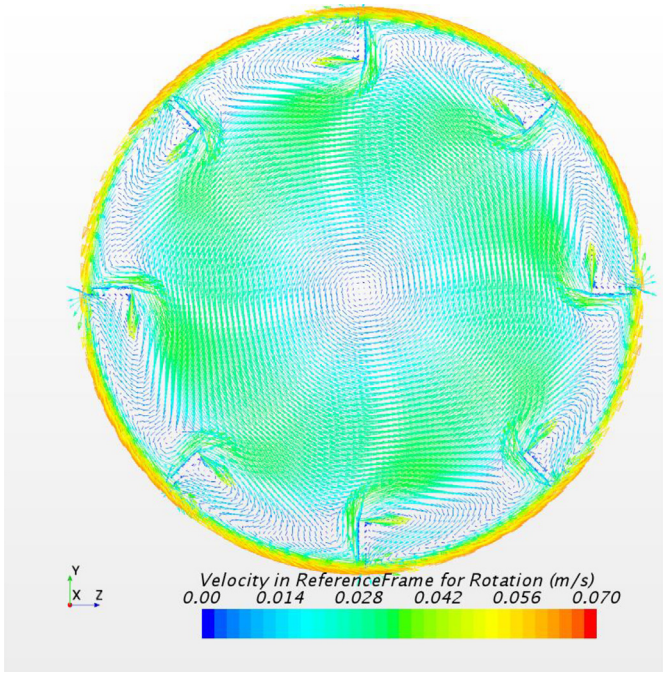

Fig. 5. Tangential air flow at x = 222 mm (3 mm grid).

aerodynamics of the drum biases the instrument to measuring only particles with d < 24 µm; similarly, the aerodynamics enhances the sensitivity of the instrument for the range 8 µm < d < 24 µm.

It is significant that the simulations predict that the rotating drum architecture is very efficient in capturing aerosolized dust; simulated dustiness = capture efficiency ~10^{-1} for particles d < 24 µm. However, experimentally, dustiness ~10^{-3}–10^{-4} (see, for example, our results in Section 5). This suggests that, in a typical dustiness experiment, most of the loaded powder consists of large agglomerates and aggregates which

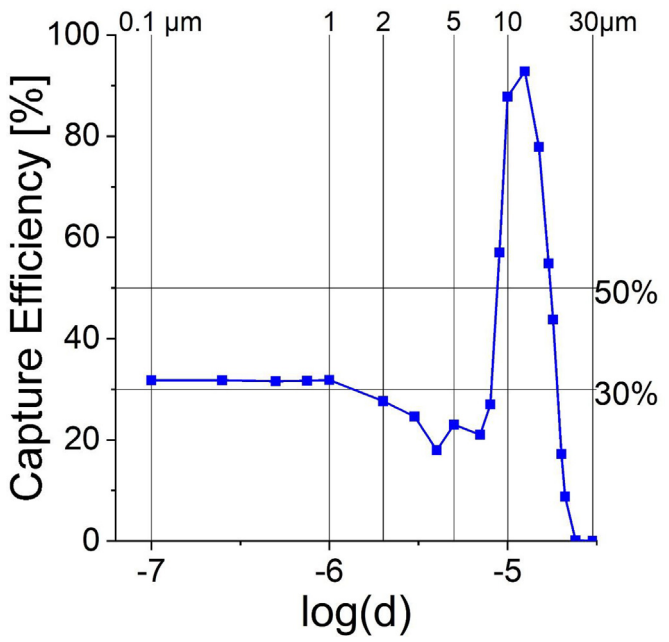

Fig. 6. Particle capture efficiency as a function of particle diameter, d.

are not aerosolized as dust. The drum is thus measuring only the small particle 'tail' of the powder particle-size distribution.

4.2.2. Particle track analysis

To investigate the particle track characteristic inside the Dustiness Drum, additional simulations were conducted with 100 particles. Particle track images were extracted and compared.

In the following three panels (Fig. 7), particle tracks are shown (a: axial view, b: side view, c: isometric view) for successive particle sizes (spherical silica particles, density ρ = 2.5 g/cm^3): top row (left-to-right): d = 100 nm, 500 nm, 1 µm; middle row (left-to-right): 5 µm, 10 µm, 12.5 µm; bottom row (left-to-right): 15 µm, 20 µm, 30 µm.

When particle diameter is less than 1 µm, particles tend to remain close to the vanes and are carried along by the flow near the vanes. Most of the particles remains trapped in the peripheral region and cannot escape. Only particles that are closest to the exit can escape.

When the particle diameter is larger than 10 µm but less than 20 µm, the particles first move with the vane and then fall from the vane into the central region of the cylindrical drum. The axial flow down the center of the drum convects these particles to the exit. Thus, this size of particles exhibits a high capture efficiency.

When the particle diameter increases to 30 µm, the gravitational force dominates, and the particles tend to fall directly onto the next vane. The transport of the particles, carried up by one vane and then falling onto the next vane, traps the particles between two vanes. As a result, these larger particles do not escape out of drum.

At the end of this article, links are provided to videos of these simulations, which illustrate these processes for representative particles of diameter d = 1 µm, 12.5 µm, 30 µm.

In a final simulation, (results not shown), the 30 µm particles were artificially released from the top of the drum, and these particles were allowed to 'fall' into the central axial flow. In this case, a small fraction located in the downstream zone, is convected out, but most of the particles do not become airborne and remain trapped within the drum by the above vane-trapping mechanism.

4.2.3. Particle distribution

In order to quantify the particle migration, we have constructed spatial histograms of the number of particles as a function of time. For the

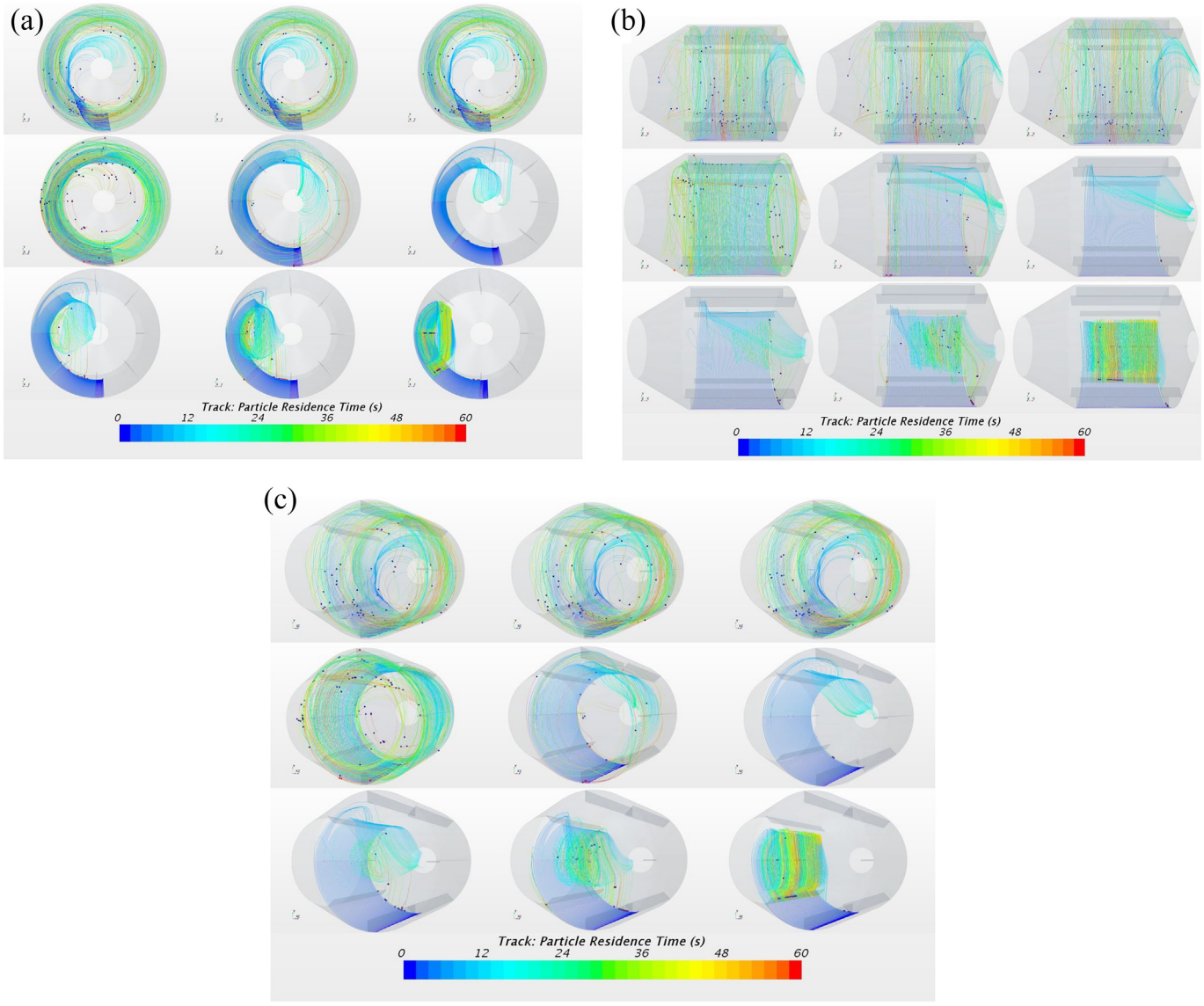

Fig. 7. Particle tracks a) axial view; b) side view; c) isometric view for successive particle sizes (spherical silica particles, density $\rho = 2.5$ g/cm^3): top row (left-to-right): d = 100 nm, 500 nm, 1 μm; middle row (left-to-right): 5 μm, 10 μm, 12.5 μm; bottom row (left-to-right): 15 μm, 20 μm, 30 μm.

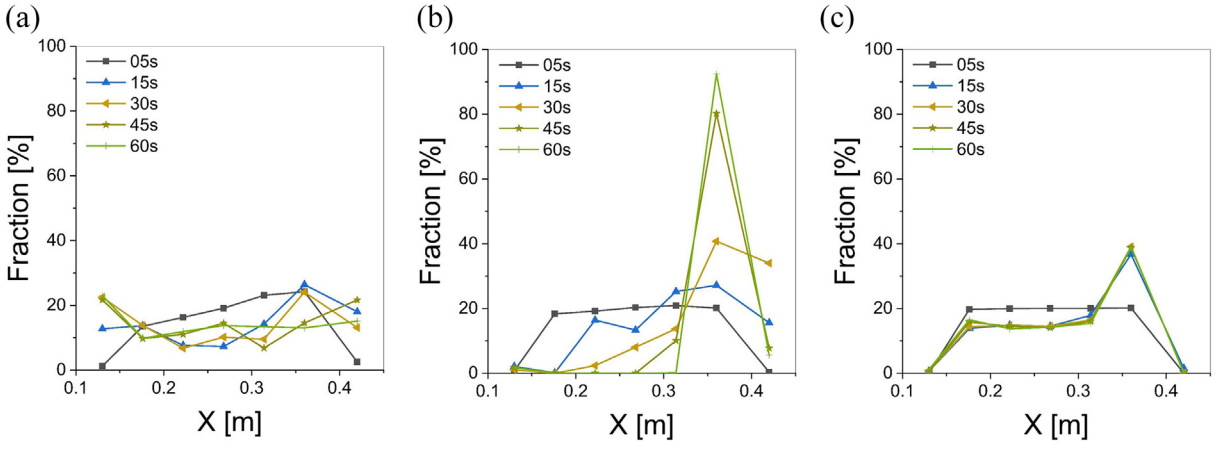

Fig. 8. Time development of horizontal particle density for several different particle sizes: a) d = 1 μm; b) d = 12.5 μm; c) d = 30 μm.

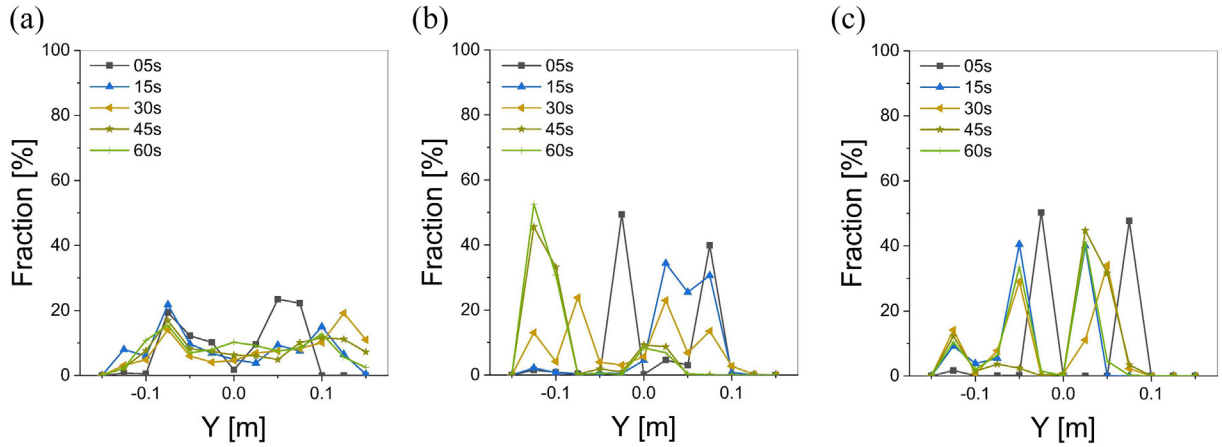

Fig. 9. Time development of vertical particle density for several different particle sizes: a) d = 1 μm; b) d = 12.5 μm; c) d = 30 μm.

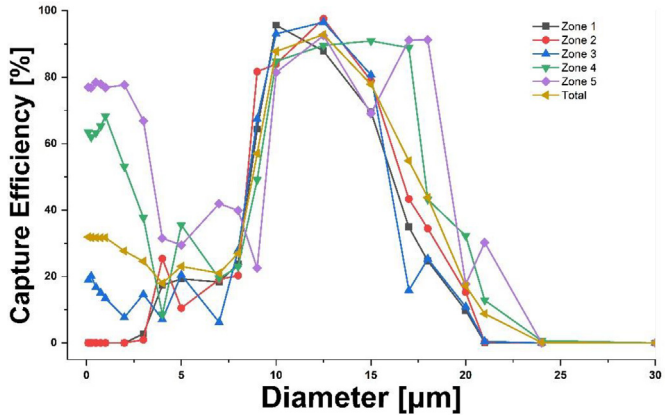

Fig. 10. Rotating drum particle capture efficiency from each zone, by particle size. (Total is the average over all 5 zones).

horizontal histograms, the drum is divided into 5 equal zones spanning the length of the barrel of the drum (i.e. the length of the vanes); there is one additional zone upstream and one downstream of the barrel, where the drum is tapered to the inlet and outlet. For the vertical histograms, the drum is divided into 13 equal slices. (Note: the central axis of the drum is y = 0; the bottom of the drum is y = −0.15 m; the top of the drum is y = +0.15 m). Particle number in each region is monitored every 5 s. Shown in the graphs are these histograms (Fig. 8 horizontal and Fig. 9 vertical) for three representative particle sizes: d = 1 μm, d = 12.5 μm; d = 30 μm. The histograms are normalized by the total number of particles remaining in the drum.

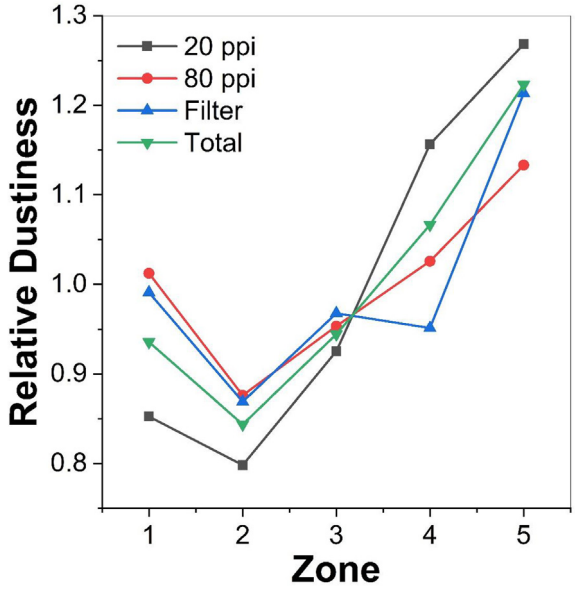

Fig. 12. Relative collection efficiency (zonal collection efficiency/ zonal average collection efficiency) by zone for each of the collected fractions.

a) Horizontal distribution of particles

The particles are initially distributed uniformly along the bottom of the drum.

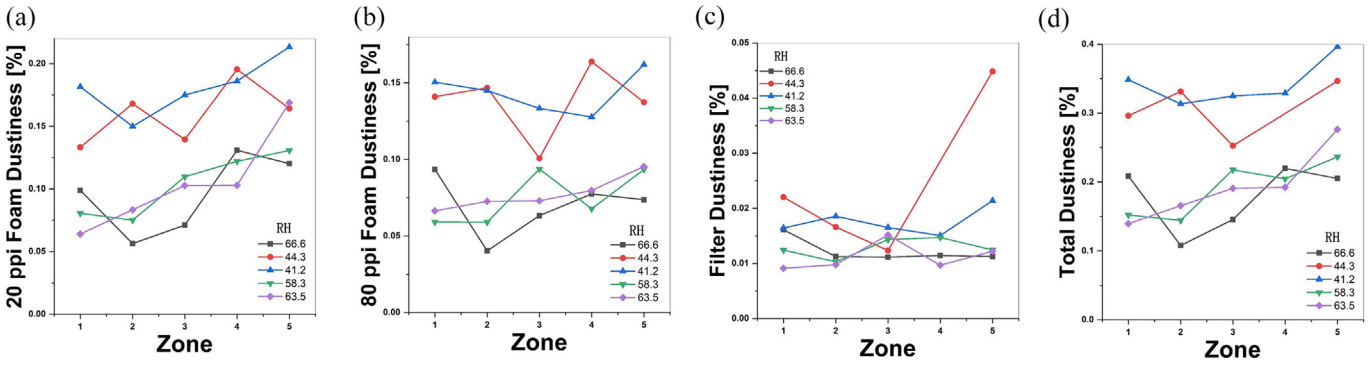

Fig. 11. Zonal collection efficiencies in the Rotating Drum for Sphericel® glass beads: a) 20 ppi foam; b) 80 ppi foam; c) filter; d) total (i.e. inhalable). RH on right side-panel.

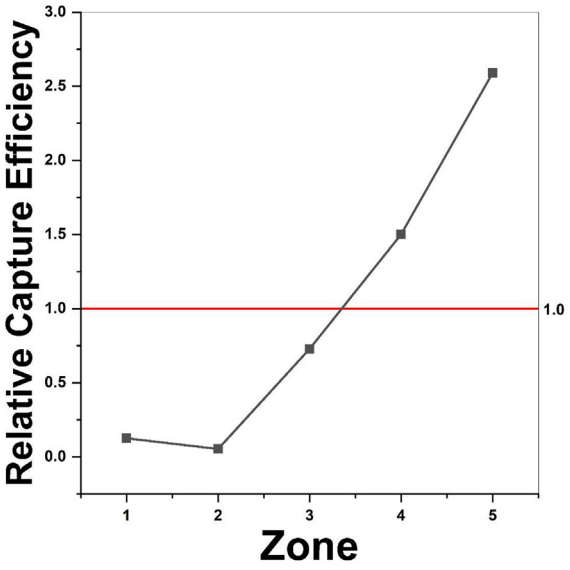

Fig. 13. Relative collection efficiency (zonal collection efficiency ratioed against the average collection efficiency over all zones) by zone, for the 5 μm 'hollow' glass sphere simulation.

For d = 1 μm, there is an initial (t = 5 s) drift downstream; then (t = 15 s, 30 s) a depletion in the center of the drum with migration towards the ends, and finally (t = 60 s) a fairly uniform distribution with an accumulation at the upstream end. The migration downstream is due to the central axial flow; the accumulation upstream is due to the backflow near the drum wall. Recall that, for this particle size, 30% of the particles have left the drum (i.e. are captured on the filter).

For d = 12.5 μm, there is a general drift downstream. This is initially gradual, but by t = 45 s, all zones except the last (nearest to the exit) have been depleted of all particles. Recall that, for this particle size, the capture efficiency is high, so this is the distribution of the very few particles that remain in the drum at the end of the experiment.

For d = 30 μm, there is a gradual drift downstream, culminating (t = 45 s) in an excess in the last zone, but without the pronounced depletion of particles from the other zones. Recall, that for this particle size, the capture efficiency is low, so that this distribution represents the spatial rearrangement with time of all the particles (since they all remain in the drum).

b) Vertical distribution of particles

Initially, all the particles are located at the bottom of the drum (y = −0.15 m). As the drum rotates, the vanes transport the particles up past the height of the drum axis (y = 0), to some higher height where the powder avalanches down. For reference, t = 15 s represents one complete revolution of the drum.

For d = 1 μm, the particles are initially (t = 5 s) clustered at two heights (y = 0.06 m and y = −0.075 m), but, as the test progresses, the particles become more evenly distributed vertically.

For d = 12.5 μm, the particles are initially (t = 5 s) clustered at two heights (y = 0.08 m and y = − 0.02 m), but, as the test progresses, these shift to the center (y = 0) and bottom (y = −0.125 m).

For d = 30 μm, the particles are initially (t = 5 s) clustered at two heights (y = 0.06 m, y = −0.075 m). and, as the test progresses, these shift slightly (y = 0.025 m, y = −0.05 m).

For the larger particles, the dust cloud is never spatially uniform.

4.2.4. Particle capture by zone

Given the richness of the spatial motion of the particles during the rotating drum test, we also examined the particle capture efficiency based on initial loading. While the standard specifies that the initial loading of the drum be uniform along the bottom of the drum, we wanted to determine whether the captured particles preferentially derive from certain initial locations.

In this set of simulations, captured particles were correlated with their initial position in the drum at the start of the experiment. This permitted a computation of capture efficiency of particles that had been initially loaded in each of the 5 zones.

Fig. 10 displays the capture efficiency for each zone as a function of particle size. For particle sizes in the range 8 μm < d < 12.5 μm, all particles, no matter their initial loading location, are captured. For smaller particles, d < 8 μm, the downstream zones (4, 5) have significantly higher capture efficiencies than do the upstream zones (1,2,3); thus, the particles that end up on the filter are dominated by particles that were loaded on the downstream portion of the drum. For larger particles, d > 12.5 μm, the furthest downstream zone (5) has the highest capture efficiency; for the largest particles, d > 20 μm, the captured particles are predominantly those that were loaded in this last zone.

5. Experimental results and discussion

The drum was zone loaded by zone with Sphericel hollow glass spheres (as described in Section 3.2). Weight gains on each of the 20 ppi and 80 ppi foams and on the final glass fiber filter were measured. Dustiness is computed as the ratio of weight gain to the mass of the initially loaded powder. Fig. 11 display these dustiness values for measurements made on 5 different days with varying humidity (RH = 66.6% on 17 May 2019; RH = 44.3% on 20 May 2019 morning; RH = 41.2% on 20 May 2019 afternoon; RH = 58.3% on 22 May 2019 morning; RH = 63.5% on 22 May 2019 afternoon). The total (i,e. inhalable) dustiness is the ratio of the total mass collected on all outlets of the drum, normalized by the mass of the initially loaded powder.

There is a general trend of a higher collection efficiency from the downstream zones. However, the large inter-day variation (presumably due to the large humidity variation) obscures this trend. If the data is presented as relative collection efficiency (namely, the ratio of zonal collection efficiency to the average collection efficiency, averaged over all zones for that day), then the trend becomes more obvious (Fig. 12). In particular, there is ~20% enhancement in the collection from the last zone relative to the zonal average.

In order to compare with our simulation work, we have performed a numerical CFD simulation (similar to those described in Section 4.2), where we have introduced 5 μm 'hollow' glass particles (ρ = 1000 kg/m^3) into the drum. We again measure zonal collection efficiency and compute a relative zonal collection efficiency, by taking the ratio with the average over all zones. The results are shown in Fig. 13.

The simulation reproduces the trend of lower collection efficiency from the upstream zones (1,2) and highest collection efficiency from the downstream zone (5). However, the simulation overpredicts the experimental variation: relatively little contribution from the upstream zones (1,2), with a 50% enhancement in zone 4 and a 160 % enhancement in zone 5.

6. Conclusions

Computational Fluid Dynamics (CFD) simulations of air flow and particle motion were carried out for the Rotating Drum dustiness test apparatus (EN15051–2 European Standard). The formation and breakup of agglomerates of smaller size particles were not incorporated in this model; similarly, particle adherence to the drum walls was also neglected. Based on observations in measuring the dustiness of many powders, we believe that the dustiness of certain classes of powders may be correlated with the powder drum wall adhesion, with low dustiness materials exhibiting high drum wall adhesion and high dustiness materials exhibiting low drum wall adhesion. It is recommended that

these neglected processes (agglomeration, break-up, drum-wall adhesion) be incorporated in future modeling of the rotating drum.

A major finding of the simulations is that the drum is very sensitive to particle size. Particles larger than d ~ 24 μm do not escape the drum, and hence do not contribute to the measured dustiness. Particles in the range 10 μm < d < 15 μm are efficiently captured at the outlet, and these particles can be expected to dominate the measured dustiness.

The CFD model overpredicts typical experimental dustiness measurements. Experimental powders invariably consist of agglomerates; these larger structures are not aerosolized and are not captured at the outlet—hence, they do not contribute to the measured dustiness.

Disclaimer

The findings and conclusions in this paper are those of the authors and do not necessarily represent the views of the National Institute for Occupational Safety and Health. Mention of any product or company name does not constitute endorsement by the Centers for Disease Control and Prevention.

Co-author responsibilities for rotating drum paper

Hongyu Chen and Milind A Jog performed the CFD simulations. Doug Evans and Leonid Turkevich conducted the rotating drum experiments. Leonid Turkevich directed the project and wrote the manuscript.

Declaration of Competing Interest

The authors declare that they have no known competing financial interests or personal relationships that could have appeared to influence the work reported in this paper.

Acknowledgments

We thank Maria Christina Kander (NIOSH and University of Cincinnati) for help with the rotating drum zonal experiments. We thank Chen Wang (NIOSH) for the scanning electron microscopy. This work is supported, in part, by the NIOSH Nanotechnology Research Center (NTRC). We thank Potters Industries LLC for their donation of the sample of Sphericel® powder used in the zonal experiments.

Appendix A. Supplementary data

Supplementary data to this article can be found online at https://doi.org/10.1016/j.powtec.2021.04.102.

References

[1] ISO, Nanomaterials—Quantification of Nano-Object Release from Powders by Generation of Aerosols, 2012 ISO TC 229 working draft (ISO TC 229/SC N–ISO/PDTS 12025).
[2] S.L. Sutter, J.W. Johnston, J. Mishima, Investigation of accident-generated aerosols: releases from free fall spills, Am. Ind. Hyg. Assoc. J. 43 (1982) 540–543.
[3] W.A. Heitbrink, P.A. Baron, K. Willeke, An investigation of dust generation by free falling powders, Am. Ind. Hyg. Assoc. J. 53 (1992) 617–624.
[4] L. Cheng, Formation of airborne-respirable dust at belt conveyor transfer points, Am. Ind. Hyg. Assoc. J. 34 (1973) 540–546.
[5] I. Pensis, J. Mareels, D. Dahmann, D. Mark, Comparative evaluation of the dustiness of industrial minerals according to European standard EN 15051 (2006), Ann. Occup. Hyg. 54 (2010) 204–216.
[6] M.A. Plinke, R. Maus, D. Leith, Experimental examination of factors that affect dust generation by using Heubach and MRI testers, Am. Ind. Hyg. Assoc. J. 53 (1992) 325–330.
[7] G. Liden, Dustiness testing of materials handled at workplaces, Ann. Occup. Hyg. 50 (2006) 437–439.
[8] W.A. Heitbrink, W.F. Todd, T.J. Fischbach, Correlation of tests for material dustiness with worker exposure from the bagging of powders, Appl. Ind. Hyg. 4 (1989) 12–16.
[9] D.H. Brouwer, I.H. Links, S.A. De Vreede, Y. Christopher, Size selective dustiness and exposure; simulated workplace comparisons, Ann. Occup. Hyg. 50 (2006) 445–452.
[10] D. Mark, The Use of Reliable Measurements of Dustiness of Chemicals in Selecting the Most Appropriate Dust Control Technology. 6th Int. Sci. Conf. Int. Occup. Hyg. Assoc. (North West Province, South Africa, 19-23 September 2005) paper S2-S3, 2005.
[11] K.L. Cashdollar, Overview of dust explosibility characteristics, J. Loss Prev. Process Ind. 13 (2000) 183–199.
[12] L.A. Turkevich, A.G. Dastidar, Z. Hachmeister, M. Lim, Potential explosion hazard of carbonaceous nanoparticles—explosion parameters of selected materials, J. Hazard. Mater. 295 (2015) 97–103.
[13] L.A. Turkevich, J. Fernback, A.G. Dastidar, P. Osterberg, Potential explosion hazard of carbonaceous nanoparticles—screening of allotropes, Combustion and Flame 167 (2016) 218–227.
[13a] A. Klippel, M. Schmidt, U. Krause, Dustiness in workplace safety and explosion protection—review and outlook, J. Loss Prev. Process Ind. 34 (2015) 22–29.
[14] C. Cowherd Jr., M.A. Grelinger, K.F. Wong, Dust inhalation exposures from the handling of small volumes of powders, Am. Ind. Hyg. Assoc. J. 50 (1989) 131–138.
[15] W.A. Heitbrink, W.F. Todd, T.C. Cooper, D.M. O'Brien, The application of dustiness tests to the prediction of worker dust exposure, Am. Ind. Hyg. Assoc. J. 51 (1990) 217–223.
[16] P. Class, P. Deghilage, R.C. Brown, Dustiness of different high-temperature insulation wools and refractory ceramic fibres, Ann. Occup. Hyg. 45 (2001) 381–384.
[17] N.O. Breum, T. Schneider, O. Joergensen, T.V. Rasmussen, S.S. Eriksen, Cellulosic building insulation versus mineral wool, fiberglass or perlite: installer's exposure by inhalation of fibers, dust, endotoxin and fire-retardant additives, Ann. Occup. Hyg. 47 (2003) 653–669.
[18] E. Petavratzi, S.W. Kingman, I.S. Lowndes, Assessment of the dustiness and dust liberation mechanisms of limestone quarry operations, Chem. Eng. Process. 46 (2006) 1412–1423.
[19] C.-J. Tsai, C.-Y. Huang, S.C. Chen, C.-E. Ho, C.-H. Huang, C.-W. Chen, C.-P. Chang, S.-J. Tsai, M.J. Ellenbecker, Exposure assessment of nano-sized and respirable particles at different workplaces, J. Nanopart. Res. 13 (2011) 4161–4172.
[20] C. Ribalta, M. Viana, A. Lopez-Lilao, S. Estupina, M.C. Minguillon, J. Mendoza, J. Diaz, D. Dahmann, E. Monfort, On the relationship between exposure to particles and dustiness during handling of powders in industrial settings, Annals of Work Exposures and Health 63 (2019) 107–123.
[21] BOHS (British Occupational Society Technology Committee Working Group on Dustiness Estimation), Dustiness Estimation Methods for Dry Materials. Technical Guide No. 4. Science Reviews Ltd, 1985.
[22] F. Hamelmann, E. Schmidt, Methods of estimating the dustiness of industrial powders a review, KONA. 21 (2003) 7–18.
[23] F. Hamelmann, E. Schmidt, Methods for characterizing the dustiness estimation of powders, Chem. Eng. Technol. 27 (2004) 844–847.
[24] F. Hamelmann, E. Schmidt, Methods for dustiness estimation of industrial powders, China Particuology 3 (2005) 90–93.
[25] ASTM, Test method for index of dustiness of coal and coke, American Society for Testing and Materials ASTM. D547–71, 1980 , (withdrawn 1986).
[26] DIN, Determination of a Parameter for the Dust Formation of Pigments and Extenders—Part 2: Drop Method. DIN 55992–2 [Deutsches Institut fuer Normung E.V. (German National Standard)], Beauth Verlag, Berlin, Germany, 1999.
[27] DIN, Determination of a Parameter for the Dust Formation of Pigments and Extenders—Part 1: Rotation Method. DIN 55992–1 [Deutsches Institut fuer Normung E.V. (German National Standard)], Beauth Verlag, Berlin, Germany, 2006.
[28] European Standard EN 15051–1, Workplace Exposure—Measurement of the Dustiness of Bulk Materials. Part 1: Requirements and Choice of Test Methods, 2013 (Comite Europeen de Normalisation, Brussels, November 2013).
[29] European Standard EN 15051–2, Workplace Exposure—Measurement of the Dustiness of Bulk Materials. Part 2: Rotating Drum Method, 2013 (Comite Europeen de Normalisation, Brussels, November 2013).
[30] European Standard EN 15051–3, Workplace Exposure—Measurement of the Dustiness of Bulk Materials. Part 3: Continuous Drop Method, 2013 (Comite Europeen de Normalisation, Brussels, November 2013).
[31] AS4156.6, Coal Preparation, Part 6: Determination of Dust/Moisture Relationship for Coal, Standards Australia, Sydney, 2000.
[32] A.H.M. Andreasen, H. Hoffman-Bang, N.H. Rasmussen, On the ability of materials to be dusty, Kolloid-Zeitschrift 86 (1939) 70–77 (in German).
[33] C.M. Hammond, Dust control concepts in chemical handling and weighing, Ann. Occup. Hyg. 23 (1980) 95–109.
[34] BOHS, Progress in dustiness estimation, Ann. Occup. Hyg. 32 (1988) 535–544.
[35] M.A. Plinke, D. Leith, D.B. Holstein, M.G. Boundy, Experimental examination of factors that affect dust generation, Am. Ind. Hyg. Assoc. J. 52 (1991) 521–528.
[36] B. Cawley, D. Leith, Bench-top apparatus to examine factors that affect dust generation, Appl. Occup. Environ. Hyg. 8 (1993) 624–631.
[37] M.A.E. Plinke, D. Leith, M.G. Boundy, F. Loeffler, Dust generation from handling powders in industry, Am. Ind. Hyg. Assoc. J. 56 (1995) 251–257.
[38] A. Lopez-Lilao, M. Bruzi, V. Sanfelix, A. Gozalbo, G. Malloi, E. Monfort, Evaluation of the dustiness of different kaolin samples, J. Occup. Environ. Hyg. 12 (2015) 547–554.
[39] A. Lopez-Lilao, A. Escrig, M.J. Orts, G. Malloi, E. Monfort, Quartz dustiness: a key factor in controlling exposure to crystalline silica in the workplace, J. Occup. Environ. Hyg. 13 (2016) 817–828.
[40] A. Lopez-Lilao, V. Sanfelix Forner, G. Malloi Gasch, E. Monfort, E. Guieno, Particle size distribution: a key factor in estimating powder dustiness, J. Occup. Environ. Hyg. 14 (2017) 975–985.
[41] K.Y. Chung, G.J. Burdett, Dustiness testing and moving towards a biologically relevant dustiness index, Ann. Occup. Hyg. 38 (1994) 945–949.
[42] K. Hjemsted, T. Schneider, Dustiness from powder materials, J. Aerosol Sci. 27 (1996) S485–S486.

[43] K. Hjemsted, T. Schneider, Documentation of a dustiness drum test, Ann. Occup. Hyg. 40 (1996) 627–643.
[44] N.O. Breum, B.H. Nielsen, E.M. Nielsen, U. Midtgaard, O.M. Poulsen, Dustiness of compostable waste: a methodological approach to quantify the potential of waste to generate airborne micro-organisms and endotoxin, Waste Manag. Res. 15 (1997) 169–187.
[45] N.O. Breum, The rotating drum tester; variability in dustiness relation to sample mass, testing time, and surface adhesion, Ann. Occup. Hyg. 43 (1999) 557–566.
[46] C.J. Tsai, C.-H. Wu, M.-L. Leu, S.-C. Chen, C.-Y. Huang, P.-J. Tsai, F.-H. Ko, Dustiness test of nanopowders using a standard rotating drum with a modified sampling train, J. Nanopart. Res. 11 (2009) 121–131.
[47] W.A. Heitbrink, Factors affecting the Heubach and MRI dustiness tests, Am. Ind. Hyg. Assoc. J. 51 (1990) 210–216.
[48] K.H. Carlson, D.R. Herman, T.F. Markey, R.K. Wolff, M.A. Dorato, A comparison of two dustiness evaluation methods, Am. Ind. Hyg. Assoc. J. 53 (1992) 448–454.
[49] S. Bach, E. Schmidt, Determining the dustiness of powders—a comparison of three measuring devices, Ann. Occup. Hyg. 52 (2008) 717–725.
[50] T. Schneider, K.A. Jensen, Combined single-drop and rotating drum dustiness test of fine to nanosize powders using a small drum, Ann. Occup. Hyg. 52 (2008) 23–34.
[51] K.A. Jensen, I.K. Koponen, P.A. Clausen, T. Schneider, J. Nanopart. Res. 11 (2009) 133–146.
[52] M.A.E. Plinke, D. Leith, R.G. Goodman, F. Loeffler, Particle separation mechanisms in flow of granular material, Part. Sci. Technol. 12 (1994) 71–87.
[53] M.A.E. Plinke, D. Leith, F. Loeffler, Cohesion in granular materials, Bulk Solids Handling 14 (1994) 101–106.
[54] J.S. Lanning, M.G. Boundy, D. Leith, Validating a model for the prediction of dust generation, Part. Sci. Technol. 13 (1995) 105–116.
[55] M. Boundy, D. Leith, T. Polton, Method to evaluate dustiness of pharmaceutical powders, Ann. Occup. Hyg. 50 (2006) 453–458.
[56] D.E. Evans, L.A. Turkevich, C.T. Roettgers, G.J. Deye, P.A. Baron, Dustiness of fine and nanoscale powders, Ann. Occup. Hyg. 57 (2013) 261–277.
[57] Turkevich, L.A., Matin, N., Ashley, E. (unpublished). 2021
[58] P. Dubey, U. Ghia, L.A. Turkevich, Computational fluid dynamics analysis of the Venturi dustiness tester, Powder Technol. 312 (2017) 310–320.
[59] N.K. Palakurthi, U. Ghia, L.A. Turkevich, , (unpublished) Particle Aerosolization from a Hill—Numerical Investigation of Aerosolization in the Venturi Dustiness Tester2021.
[60] A. Sharma, U. Ghia, L.A. Turkevich, Large Eddy Simulation of Flow Over a Hemispherical Obstacle Within a Cylindrical Tube. Proceedings of FEDSM 2020, ASME, 2020 paper 10596.
[61] A. Sharma, U. Ghia, L.A. Turkevich, Effect of Vortex Shedding on the Aerosolization of a Particle from a Hill using Large Eddy Simulation. Proceedings of the 2020 AIAA Aviation Forum, AIAA, 2020 paper 3339120.
[62] Evans, D.E. & Turkevich, L.A. (unpublished). 2021
[63] L. Prigozhin, H. Kalman, Radial mixing and segregation of a binary mixture in a rotating drum: model and experiment, Phys. Rev. E 57 (2) (1998) 2073–2080.
[64] J. McCarthy, T. Shinbrot, G. Metcalfe, E. Wolf, J.M. Ottino, Mixing of granular materials in slowly rotated containers, AIChEJ 42 (1996) 3351–3363.
[65] S.K. Hajra, T. Bhattacharya, J.J. McCarthy, Improvement of granular mixing of dissimilar materials in rotating cylinders, Powder Technol. 198 (2010) 175–182.
[66] T. Ward, W. Hourigan, Granular segregation in a tilted rotating drum, Powder Technol. 215-216 (2012) 227–234.
[67] C.-C. Liao, S.-F. Ou, S.-L. Chou, Y.-R. Chen, Influence of fine powder on dynamic properties and density segregation in a rotating drum, Adv. Powder Technol. 31 (2020) 1702–1707.
[68] S. Deng, Z. Wen, F. Su, Z. Wang, G. Lou, X. Liu, R. Dou, Radial mixing of metallurgical slag particles and steel balls in a horizontally rotating drum: a discussion of particle sie distribution and mixing time, Powder Technol. 378A (2021) 441–454.
[69] O. Zik, D. Levine, S. Lipson, Rotationally induced segregation of granular materials, Phys. Rev. Lett. 73 (1994) 644–647.
[70] S. Chakraborty, P.R. Nott, J.R. Prakash, Analysis of radial segregation of granular mixtures in a rotating drum, European Physical J. E 1 (2000) 265–273.
[71] I. Zuriguel, J. Peisanho, T. Mullin, Segregation pattern competition in a thin rotating drum, Phys. Rev. E 79 (2008) 1–5.
[72] Z. Hou, Y. Zhao, Numerical and experimental study of radial segregation of bidispersic particles in a quasi-two-dimensional horizontal rotating drum, Particuology 51 (2020) 109–119.
[73] B. Yari, C. Beaulieu, P. Sauriol, F. Bertrand, J. Chaouki, Size segregation of bidisperse granular mixtures in a rotating drum, Powder Technol. 374 (2020) 172–184.
[74] E. Alizadeh, O. Dube, F. Bertrand, J. Chaouki, Characterization of mixing and size segregation in a rotating drum by a particle tracking method, AIChEJ 59 (2013) 1894–1905.
[75] M.M.H.D. Arutz, H.H. Beeftink, W.K. Otter, W.J. Briels, R.M. Bowen, Segregation of granular particles by mass, radius and density in a horizontal rotating drum, AIChEJ 60 (2013) 50–59.
[76] D. Khakhar, V. Ashish, S. Orpe, S.K. Hajra, Segregation of granular materials in rotating cylinder, Physica A 318 (2003) 129–136.
[77] N. Olivitran, N. Fraysse, P. Girard, M. Ramanda, D. Chatain, Modeling and simulations of the behavior of glass particles in a rotating drum in heptane and water vapor atmospheres, Europ. Phys. J. B 15 (2002) 217–222.
[78] Y. Liu, M. Gonzalez, C. Wassgren, Modeling granular material blending in a rotating drum using a finite element method and advection-diffusion equation multi-scale model, AIChEJ 64 (2018) 3277–3292.
[79] S. Yang, A. Cahyadi, J. Wang, J.W. Chew, DEM study of granular flow characterization in the active and passive regions of a three-dimensional rotating drum, AIChEJ 62 (2016) 3874–3888.
[80] S. Yang, L. Zhang, K. Luo, J.W. Chew, DEM investigation of the axial dispersion behavior of a binary mixture in the rotating drum, Particle Technol. 330 (2018) 93–104.
[81] Q. Zheng, A. Yu, Modeling the granular flow in a rotating drum by the Eulerian finite element method, Powder Technol. 286 (2015) 361–370.
[82] E. Alizadeh, F. Bertrand, J. Chaouki, Comparison of DEM results and Lagrangian experimental data for the flow and mixing of granules in a rotating drum, AIChEJ 60 (2013) 60–75.
[83] M.A. Delele, F. Weigler, G. Franke, J. Mellmann, Studying the solids and fluid flow behavior in rotating drums based on multiphase CFD model, Particle Technology 292 (2016) 260–271.
[84] D.A. Santos, C.R. Duarte, M.A.S. Barrozo, Segregation phenomenon in a rotating drum: experimental study and CFD simulation, Powder Technol. 294 (2016) 1–10.
[85] S. Yang, Y. Suu, L. Zhang, J.W. Chew, Numerical study on the axial segregation dynamics of a binary size granular mixture in a three-dimensional rotating drum, Phys. Fluids 29 (2017) 103302.
[86] A. Boateng, P.V. Barr, Modelling of particle mixing and segregation in the transverse plane of a rotary kiln, Chem. Eng. Sci. 51 (1996) 4167–4181.
[87] W. Rong, B. Li, Y. Feng, P. Schwarz, P. Witt, F. Qi, Numerical analysis of size-induced particle segregation in rotating drums based on Eulerian continuum approach, Powder Technol. 376 (2020) 80–92.
[88] A.N. Huang, T.H. Cheng, W.Y. Hsu, C.C. Huang, H.P. Kuo, DEM study of particle segregation in a rotating drum with internal diameter variations, Powder Technol. 378A (2021) 430–440.
[89] R.J. Brandao, R.M. Lima, R.L. Santos, C.R. Duarte, M.A.S. Barrozo, Experimental study and DEM analysis of granular segregation in a rotating drum, Powder Technol. 364 (2020) 1–12.
[90] D. Khakhar, V. Ashish, J. Orpe, J.M. Ottino, Continuum model of mixing and segregation in a rotating cylinder: concentration-flow coupling and streak formation, Powder Technol. 116 (2001) 232–245.
[91] I. Frew, P.W. Wypych, L. Mar, Different Modes of Dust Testing for Bulk Solids, Proceedings 11th International Congress on Bulk Materials Storage, Handling and Transportation, 2-4 July 2013 The University of Newcastle, Australia, 2013.
[92] S. Wangchai, D.B. Hastie, P.W. Wypych, The Simulation of Particle Flow Mechanisms in Dustiness Testers, Proceedings 11th International Congress on Bulk Materials Storage, Handling and Transportation, 2-4 July 2013 the University of Newcastle, Australia, 2013.
[93] S. Wangchai, D.B. Hastie, P.W. Wypych, The investigation of particle flow mechanisms of bulk materials in dustiness testers, Part. Sci. Technol. 34 (2016) 241–254.
[95] P. Wypych, L. Mar, Investigations into the dustiness of bulk materials, Australian Bulk Handling Review 18 (2013) 64–67.
[96] Chen, H., Jog, M.A., Turkevich, L.A. (unpublished). 2021
[97] L. Schiller, A. Naumann, Ueber die grundlegenden Bereichnungen bei der Schweckraftaufbereitung, VDI Zeits. 77 (1933) 318–320.
[98] I.B. Celik, U. Ghia, P.J. Roache, C.j. Freitas, P.E. Raad, Procedure for estimation and reporting of uncertainty due to discretization in CFD applications, J. Fluids Eng. 130 (2008), 078001, .
[99] S. Wangchai, D.B. Hastie, P.W. Wypych, Particle size segregation of bulk material in dustiness testers via DEM simulation, Particulate Science & Technology 36 (2016) 20–28.